ZERO THEORY RESEARCH PROGRAM / IRCBHC

Local Wave Geometry, Operational Units, and CMB Temperature Comparison

Delayed Pursuit, Transverse-Pair Transport, and Observer Readouts

S. M. H. Emamifar
ORCID: 0009-0007-6257-0163
Zero Theory Research Program / IRCBHC

Research manuscript v0.9.3 | 16 November 2026

Abstract

We present a calculable local-wave construction in Zero Theory and evaluate its geometrical, operational, and cosmological consequences. A transverse rotating pair yields exact orthogonality and derivative identities; an explicitly specified traveling phase produces first-order transport along one local characteristic. A reference wavelength and the completion period of that wave provide operational length and duration units, while an observer model separates spatial phase profiles from temporal cycle readouts. For perpendicular rigid rings joined at two poles, exact quarter-cycle-delayed return to an earlier location imposes a closed-form orientation-increment condition. A selected feedback law reduces the mean modeled positional mismatch by 86.3% over two cycles. A mirrored two-structure construction with antiparallel, inward-facing axes reproduces the spatial matching and symmetry identities to numerical precision. A constant-pitch-angle helix further gives a geometric pitch–radius relation. With the specified wave-pitch correspondence and blackbody occupation transport, the model yields the temperature relation $T_{\mathrm{CMB}}(z) = T_0(1 + z)$. Its fixed-normalization evaluation against 45 published reconstructed temperatures finds 45/45 entries within two quoted standard uncertainties, with descriptive diagonal residual sum $Q_{\mathrm{diag}} = 25.403$. An input-parity audit separates the empirical temperature normalization and measured redshifts from the 45 held-out temperature estimates, and compares these inputs with the standard temperature-law calculation. The complete observational table, uncertainty convention, source references, and executable calculations are supplied. The results establish a reproducible local-wave framework and a positive temperature–redshift compatibility check, with the physical identification of the geometric variables stated as part of the modeling scope.

Keywords: emergent spacetime; intrinsic wave units; transverse transport; hinged-ring geometry; delayed pursuit; observer readout; CMB temperature–redshift relation; Zero Theory.

1 Introduction

The physical meaning of distance and duration can be investigated through internally repeatable processes rather than by assuming an external ruler or clock. The Zero Theory research program approaches this question using structured local wave configurations. The present paper develops a concrete mathematical setting for these configurations and tests selected outcomes, including an observational temperature–redshift relation.

Three linked questions organize the study. What relations follow from an orthogonal rotating transverse pair? What orientation is required when a delayed marker returns to the earlier position of a second marker in a two-pole geometry? And how can wave-defined length and duration units,

together with a helical wavelength correspondence, be related to observer records and to published cosmic microwave background (CMB) temperature measurements?

We answer these questions through analytic geometry, first-order transport identities, reproducible numerical checks and a 45-entry observational comparison. The numerical comparison uses the published redshifts and a fixed present-day temperature normalization, without fitting the 45 distant temperature values. Model definitions, calculated consequences and observational inputs are distinguished in the relevant methods sections. The local constructions are intended as a mathematically explicit component of the broader Zero Theory program, whose more extensive particle and cosmological developments are outside this paper's scope.

2 Relation to other emergence approaches

There is a substantial literature in which spacetime or field behavior is regarded as nonprimitive. These programs differ markedly in which structures they retain at the outset. In causal set theory, the fundamental data are a locally finite partial order; continuum causal order and volume are targets of reconstruction [2]. In group field theory condensates, an effective cosmological geometry is pursued from collective quantum-geometric degrees of freedom above a "no-space" vacuum [3]. In holographic accounts, entanglement in a lower-dimensional quantum theory is related to geometrical connectedness of the bulk description [4].

Relational-clock approaches address a more directly adjacent *measurement* question: Page and Wootters describe dynamics conditionally on internal clock readings [5]; Rovelli analyzes relational and partial observables [6]. Separately, string-net models exhibit emergent low-energy gauge and fermionic excitations [7]; they illustrate a complementary route from microscopic degrees of freedom to effective fields.

Table 1: Representative approaches to emergent spacetime and fields, compared by their starting structures and research targets.

Program	Starting structure	What is pursued or achieved within its own scope
Causal sets [2]	Locally finite causal order	A continuum spacetime approximation from order and counting; continuum and dimension-sensitive reconstruction are investigated.
GFT condensates [3]	Quantum-geometric degrees of freedom	Collective effective cosmological evolution; observables and clock choices require specification.
Holographic emergence [4]	Entanglement in a boundary quantum theory	Geometric connectedness of bulk spacetime within a boundary-theory setting.
Relational time [5, 6]	Quantum correlations / physical observables	Conditional time and relational observables.
String-net emergence [7]	Local bosonic/spin models	Effective gauge and fermionic excitations from local microscopic degrees of freedom.
Present TFPT construction	Local transverse pair, assigned phase and computational chart	Pair geometry, axial transport identities, wave-defined units, and observer phase readouts.

The comparison highlights the starting ingredients of each approach. Zero Theory here begins with a declared local wave pair and investigates the geometry of recurrence, the associated operational units, and their relation to observer records. This focus is closest in measurement questions to relational-clock research, while its interest in emerging effective fields parallels other constructive programs.

2.1 Comparison of starting structures and empirical-input roles

A comparison of "few starting assumptions" and a comparison of "few measured inputs" ask different questions. The former concerns mathematical or physical premises of the constructive theory; the latter concerns empirical quantities supplied before a specified observable is computed. Table 2 makes this distinction explicit for the cited publications, at the scope at which they are used in this paper. A structural premise is not an empirical calibration simply because it may eventually have observational consequences. Likewise, a computational coordinate chart is a mathematical input, not an additional measured constant.

Table 2: Representative input accounting for the *cited constructions*. The table is a comparison of scope and input type, not a numerical ranking of complete research programs.

Program	Theoretical starting structure in the cited work	Role of measured inputs in that construction
Causal sets [2]	Locally finite causal partial order; dynamics/continuum approximation are further research components.	No measured T_0 or source redshift is needed to *define* a causal set; the cited review is not the same 45-point CMB temperature calculation.
GFT condensates [3]	Group-field degrees of freedom, quantum dynamics and a condensate description.	Model interactions and state choices belong to the theoretical construction; the cited review develops effective cosmology rather than the specific 45-temperature audit.
Holographic emergence [4]	Boundary quantum description and an entanglement structure.	The cited argument concerns bulk connectedness, without an input list or prediction for the CMB $T(z)$ dataset analyzed here.
Relational time [5, 6]	Quantum correlations, internal-clock/observable structure and conditional descriptions.	Clock and state assignments are conceptual/model inputs; the cited papers do not use the 45 reconstructed CMB temperatures.
String-net emergence [7]	Microscopic bosonic or spin degrees of freedom and their many-body dynamics.	Hamiltonian/microscopic choices set the model; the cited work does not evaluate this CMB temperature observable.
Present local Zero Theory construction	Orthogonal wave-pair geometry; selected ordered phase, hinge, and wave–pitch correspondence.	Exact geometry uses no CMB data. The CMB application inputs measured T_0 and each observed z_i; the 45 remote T_i values are reserved for comparison.

The five other approaches have different observables and explanatory goals. Their absence from the specific CMB calculation *in the cited works* therefore does not count as an empirical failure or a larger input burden. An empirical-input comparison becomes quantitative only after two models have been assigned the same observable, frames, accuracy, and data-use protocol. The directly matched CMB comparison is given in Section 10.2.

3 Model definitions and calculation strategy

The model is specified by an orthogonal transverse pair, a mathematical calculation frame, and an ordered phase parameter. The transport study selects a traveling-wave phase. The ring study specifies perpendicular planes, shared polar hinges, a quarter-cycle delay and a local matching criterion. Within these inputs we calculate orthogonality identities, a delayed orientation requirement, and observable readout conventions. We use "creation and "deletion to name the red and blue roles in the ring interpretation; the equations in this paper quantify their geometric motion.

The geometrical developments below stand independently of a particular large-scale counter-rotation history. They use a local frame to exhibit relations between phase, orientation, position

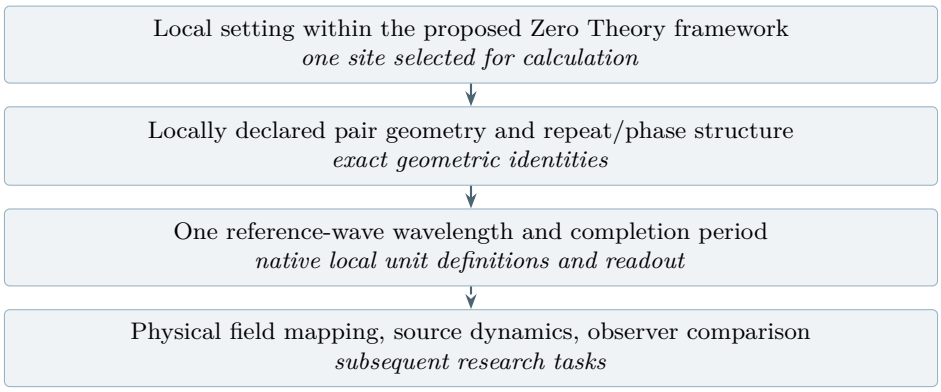

Figure 1: Organization of the local construction. Solid arrows denote the mathematical sequence developed here; the dashed arrow identifies the proposed physical extension.

and recurrence. Their physical interpretation is considered after the mathematical results have been established.

4 Transverse-pair geometry and rotation identities

Let $\mathbf{n}$ be an axial unit direction and $(\mathbf{e}_1, \mathbf{e}_2)$ an orthonormal basis of the computational transverse plane. Define

$$\begin{aligned} \mathbf{u}(\theta) &= \mathbf{e}_1 \cos\theta + \mathbf{e}_2 \sin\theta, \\ \mathbf{v}(\theta) &= -\mathbf{e}_1 \sin\theta + \mathbf{e}_2 \cos\theta, \\ \mathbf{F} &= A\mathbf{u}(\theta), \qquad \mathbf{G} = B\mathbf{v}(\theta). \end{aligned} \tag{1}$$

The abstract transverse quantities $\mathbf{F}, \mathbf{G}$ have independently specified amplitudes A, B. Their operational identification with electromagnetic fields is considered separately. For nonzero amplitudes,

$$\mathbf{F} \cdot \mathbf{G} = 0, \qquad \mathbf{n} \cdot \mathbf{F} = \mathbf{n} \cdot \mathbf{G} = 0, \qquad \|\mathbf{F}\|^2 = A^2, \quad \|\mathbf{G}\|^2 = B^2. \tag{2}$$

The quarter-turn operator J in this transverse basis satisfies $J^2 = -I$ and $\mathbf{v} = J\mathbf{u}$. Hence, with constant nonzero amplitudes and any differentiable phase,

$$\frac{d\mathbf{F}}{dq} = \theta'(q)\frac{A}{B}\mathbf{G}, \qquad \frac{d\mathbf{G}}{dq} = -\theta'(q)\frac{B}{A}\mathbf{F}. \tag{3}$$

Equations (2)–(3) follow from the orthogonal basis and a differentiable phase, independently of its detailed progression. For variable amplitudes, the derivatives acquire the terms $(dA/dq)\mathbf{u}$ and $(dB/dq)\mathbf{v}$. Determining A/B, the phase evolution, and the associated energy requires additional physical input.

5 Delayed pursuit in a two-pole ring geometry

A complementary interpretation assigns two successive roles to the geometry: a red marker denotes an initial local event (“creation”), and a blue marker represents an event intended to revisit its location after a quarter-cycle (“deletion”). In this article these terms name modeled functions rather than measured field processes. The idea motivates a precise question: under what orientation history can a delayed marker reach the earlier spatial position of another?

The model uses two perpendicular circular tracks joined at two fixed poles, a prescribed lag of $\delta = \pi/2$, and strictly local matching of the blue marker to a prior red location. The local-matching

rule is an input to the calculation. As the rings reorient about their common pole-to-pole axis, the condition for matching can be derived explicitly."

5.1 An explicit rigid-hinge representation

For one restricted calculable realization, let two radius-R circular rings remain rigid, share the fixed poles $(0, 0, \pm R)$, and have perpendicular planes at all modeled instants. Their common azimuthal reorientation is $\alpha(s)$ about the pole-to-pole axis, where s is a *preassigned ordered phase label* (not emergent physical time). Define a point on either ring by

$$\mathbf{P}(\varphi, \gamma) = R\,(\sin\varphi\cos\gamma,\ \sin\varphi\sin\gamma,\ \cos\varphi)\,. \tag{4}$$

With quarter-cycle lag $\delta = \pi/2$, a red trajectory, blue trajectory and the red trace targeted by blue are respectively

$$\begin{aligned} \mathbf{r}(s) &= \mathbf{P}(s, \alpha(s)), \\ \mathbf{b}(s) &= \mathbf{P}(s-\delta, \alpha(s)+\pi/2), \\ \mathbf{r}_{\text{old}}(s) &= \mathbf{P}(s-\delta, \alpha(s-\delta)). \end{aligned} \tag{5}$$

The ring planes are perpendicular by construction. These geometric trajectories are modeled separately from the field-like vectors $\mathbf{F}, \mathbf{G}$ of Eq. (1), making the distinction between a point's position and a field vector explicit.

5.2 Exact condition for revisiting a previous creation site

Define the spatial mismatch $D(s) = \|\mathbf{b}(s) - \mathbf{r}_{\text{old}}(s)\|$ and the orientation difference $\Delta(s) = \alpha(s) + \pi/2 - \alpha(s-\delta)$. Direct Euclidean algebra yields

$$D^2(s) = 2R^2 \sin^2(s-\delta)\,[1 - \cos\Delta(s)]\,. \tag{6}$$

At any *nonpolar* phase, exact spatial coincidence is therefore equivalent to

$$\boxed{\alpha(s) - \alpha(s-\delta) = -\pi/2 \pmod{2\pi}.} \tag{7}$$

For locked rings, $\alpha(s) \equiv 0$, the mismatch is $D(s) = \sqrt{2}R|\sin(s-\delta)|$. Thus, within the rigid perpendicular geometry and local matching rule, reorientation is required for coincidence at all nonpolar sites; coincidence at the shared poles occurs independently of the reorientation.

One exact solution is $\alpha(s) = -s + \alpha_0$, corresponding to a -90° orientation change per quarter-cycle. The relation permits multiple orientation histories: for example, $\alpha(s) = -s + 0.2\sin(4s)$ also satisfies Eq. (7), as do alternative winding branches. The constraint therefore selects a delayed angular *increment*, while a dynamical law would be needed to select one particular motion.

5.3 Pursuit response and numerical comparison

To explore a response to the mismatch, we specify a gradient-based controller for the hinge angle. Let $U(s) = D^2(s)/2$; taking the negative derivative with respect to the current hinge angle gives

$$\frac{d\alpha}{ds} = -KR^2 \sin^2(s-\delta)\sin[\alpha(s) + \pi/2 - \alpha(s-\delta)]\,, \qquad K = 12,\ R = 1. \tag{8}$$

Here K is a selected dimensionless gain and $\alpha(s \le 0) = 0$ sets the initial history. The controller provides an explicit numerical response model; it is independent of the preceding geometric matching identity and represents one possible mechanism for lowering positional error.

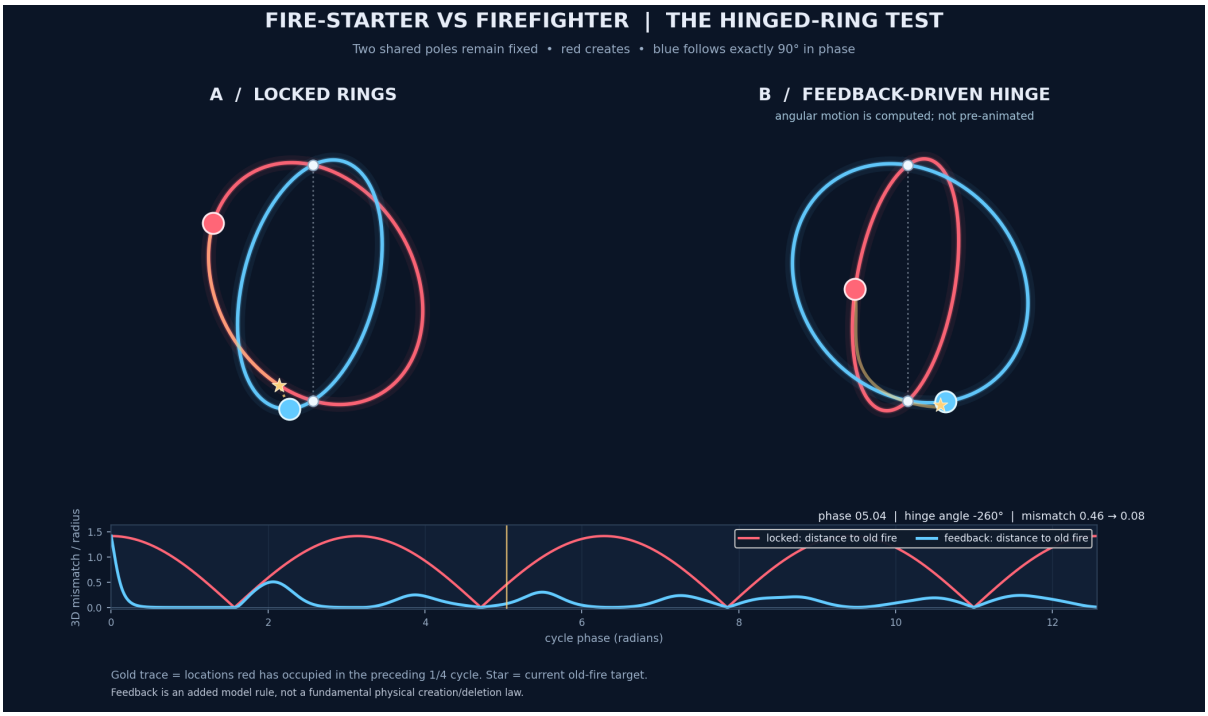

Figure 2: Two modeled ring configurations: locked planes (left) and a hinge controlled by delayed positional error (right). Red denotes the initial location, blue the delayed participant, and gold the target. The trace below compares positional mismatch in units of ring radius. Reproduction code accompanies the source archive.

Over two phase cycles, the archived run yields mean mismatch $0.90055R$ for locked rings and $0.12370R$ under Eq. (8), a reduction of 86.3%. A residual mismatch remains. The $K = 0$ control keeps the rings stationary, while independent symbolic and numerical checks reproduce Eq. (6), the $\alpha = -s$ solution, and nonuniqueness of the matching trajectory. These findings characterize the selected response rule rather than independently fixing a physical torque law.

5.4 Facing-axis geometry of two mirror structures

We next consider two complete ring structures arranged face-to-face. Each directed hinge axis points toward the opposite structure, so their supporting lines coincide while their directions are antiparallel. This author-corrected orientation extends the single-hinge study of Eqs. (4)–(7) to a mirror-related pair.

To make the correction reproducible, introduce the *computational* label $\sigma = +1$ for the left structure and $\sigma = -1$ for the right, the arbitrary half-separation $d > R$, and orthonormal local frames:

$$\begin{aligned} \mathbf{C}_\sigma = (-\sigma d, 0, 0), \quad \mathbf{n}_\sigma = (\sigma, 0, 0), \\ \mathbf{e}_{1\sigma} = (0, 0, -\sigma), \quad \mathbf{e}_{2\sigma} = (0, 1, 0), \quad \mathbf{e}_{1\sigma} \times \mathbf{e}_{2\sigma} = \mathbf{n}_\sigma. \end{aligned} \tag{9}$$

Consequently $\mathbf{n}_+ \cdot \mathbf{n}_- = -1$ while $\mathbf{n}_\sigma \cdot (\mathbf{C}_{-\sigma} - \mathbf{C}_\sigma) = 2d > 0$: both directed axes face the opposite center. The offset d sets the scale of the geometric display.

Let each complete structure carry two radius-R circular tracks, with its common poles at $\mathbf{C}_\sigma \pm R\mathbf{n}_\sigma$. The following global-coordinate parameterization uses each structure's *own* right-handed local frame:

$$\mathbf{P}_\sigma(\phi, \beta) = \mathbf{C}_\sigma + R\left[\cos\phi\, \mathbf{n}_\sigma + \sin\phi\,(\cos\beta\, \mathbf{e}_{1\sigma} + \sin\beta\, \mathbf{e}_{2\sigma})\right]. \tag{10}$$

For a shared ordered phase label ϑ, define the red marked point, blue marked point, and earlier

red location by

$$\begin{aligned} \mathbf{r}_\sigma(\vartheta) &= \mathbf{P}_\sigma(\sigma\vartheta, -\sigma\vartheta), \\ \mathbf{b}_\sigma(\vartheta) &= \mathbf{P}_\sigma(\sigma(\vartheta-\delta), -\sigma\vartheta + \sigma\delta)\,, \\ \mathbf{r}_{\sigma,\mathrm{old}}(\vartheta) &= \mathbf{P}_\sigma(\sigma(\vartheta-\delta), -\sigma(\vartheta-\delta))\,, \\ \delta &= \pi/2. \end{aligned} \tag{11}$$

Equations (10)–(11) give $\mathbf{b}_\sigma(\vartheta) = \mathbf{r}_{\sigma,\mathrm{old}}(\vartheta)$ identically. The two ring planes differ by $\sigma\pi/2$ in azimuth and are perpendicular at every modeled phase; their polar junctions remain fixed. The red trajectories carry opposite signed local phases, $+\vartheta$ and $-\vartheta$, and the reflection $M(x, y, z) = (-x, y, z)$ maps the left geometry onto the right. This is an explicit mirror and pursuit construction with a selected angular schedule.

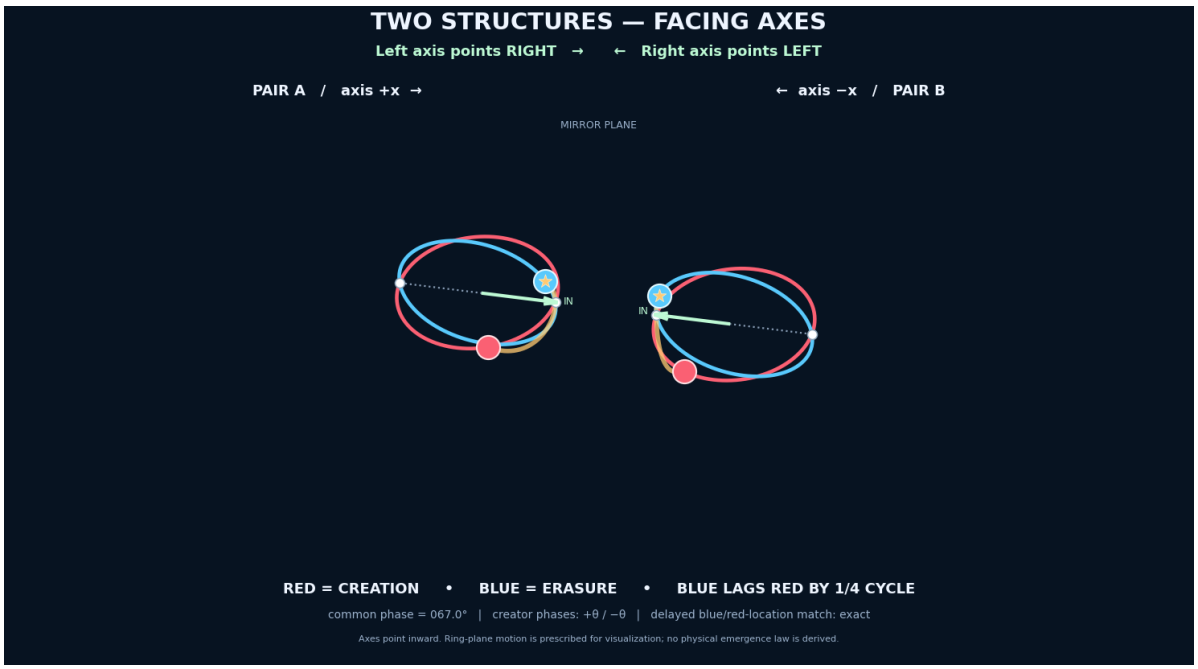

Figure 3: Facing-axis mirror arrangement. Left and right hinge axes point inward, with directed dot product -1. Each structure contains perpendicular red and blue planes meeting at two poles. The displayed phase schedule implements exact delayed-location matching. Source: corrected facing-axis v3 code archive.

The numerical replay verifies axis opposition, inward pointing, mirror equality, delayed matching, plane orthogonality and stable polar junctions. Mirror and positional residuals are zero; perpendicularity errors are about 5×10^{-16} in floating-point arithmetic. The earlier codirected display (axis cosine $+1$) is retained as a regression control against the corrected cosine -1. Since $\beta_\sigma(\vartheta) = -\sigma\vartheta$ is specified in Eq. (11), the check establishes consistency of the chosen kinematics. The phase label ϑ remains a computational ordering parameter.

5.5 Connecting ring trajectories with the transverse pair

The ring and field-pair constructions address complementary geometric descriptions. Equation (10) tracks marked positions and ring planes, whereas Eq. (1) defines the orientation and magnitude of two transverse vectors. A physical synthesis would require a map $\mathcal{M} : \{\mathbf{P}_\sigma, \mathbf{r}_\sigma, \mathbf{b}_\sigma\} \mapsto \{\mathbf{F}, \mathbf{G}\}$ and, ultimately, a connection to instrument-defined electromagnetic observables $\mathbf{E}, \mathbf{B}$. That mapping would also have to specify source response, phase dynamics, energy flow and the relevant frame transformations. The equations developed here provide explicit geometric data for such a construction.

5.6 Symmetry and interpretation

The model exhibits three distinct relations: orthogonality of ring planes, delayed correspondence of marked locations, and mirror symmetry between the two structures. These relations support the proposed pursuit interpretation in geometric terms. Establishing a physical creation–deletion balance would additionally require a defined quantity, its persistence and removal rules, and a conservation or exchange equation. The measured **E** and **B** components also transform between reference frames [13]; the abstract $\mathbf{F}, \mathbf{G}$ description is maintained until a corresponding operational field map is specified.

6 Phase transport and local wave units

Introduce dimensionless labels τ (ordered cycle progression) and ξ (axial phase offset). In the *restricted uniform construction*, choose

$$\theta(\xi, \tau) = 2\pi(\tau - \xi) + \theta_0. \tag{12}$$

For A, B independent of ξ, τ, differentiating Eq. (1) yields the Hadi/TFPT local transport identities

$$(\partial_\tau + \partial_\xi)\mathbf{F} = 0, \qquad (\partial_\tau + \partial_\xi)\mathbf{G} = 0. \tag{13}$$

Equations (13) express transport along the characteristic selected by Eq. (12). The transverse orthogonality identities hold more generally; the propagating phase fixes this particular transport behavior. A source model and dynamical energy law would be required to determine the phase progression independently.

The author defines a local physical ruler from one reference wave. Let ℓ_* denote its wavelength and P_* the duration of completion of the *same* wave. In a locally uniform comparison chart,

$$\xi = x/\ell_*, \qquad \tau = t/P_*, \qquad v_{\text{phase}} = \ell_*/P_*. \tag{14}$$

The speed expressed *in those same native units* is the exact unit identity

$$\boxed{v_{\text{native}} = \frac{\ell_*/\ell_*}{P_*/P_*} = 1 \text{ step/tick.}} \tag{15}$$

The value 1 is the speed in the chosen wave-owned units; it follows by defining one step as ℓ_* and one tick as P_*. The project's provisional local-wave wavelength is $\text{Gam}_L = 8.86 \times 10^{-22}\,\text{m}$. Its corresponding SI-calibrated reporting period is

$$\text{Tick}_L = \text{Gam}_L/c_{\text{cal}} \simeq 2.95538 \times 10^{-30}\,\text{s}, \quad c_{\text{cal}} = 299\,792\,458\,\text{m/s}. \tag{16}$$

Here c_{cal} supplies the SI conversion, rather than emerging from the transverse-pair equations. The wavelength alone does not fix A/B. When comparing observers, both reference units and the transformation of field components and derivatives must be specified. This separates the local operational convention from an eventual observer-independent physical prediction.

7 Observer readouts and cycle counting

The STEP01 archive illustrates two complementary readouts. A depth-cue animation emphasizes near/far positions relative to an observer along $+x$. The wave-readout figure compares a transverse spatial profile at a fixed instant with the component record at a fixed location. For this

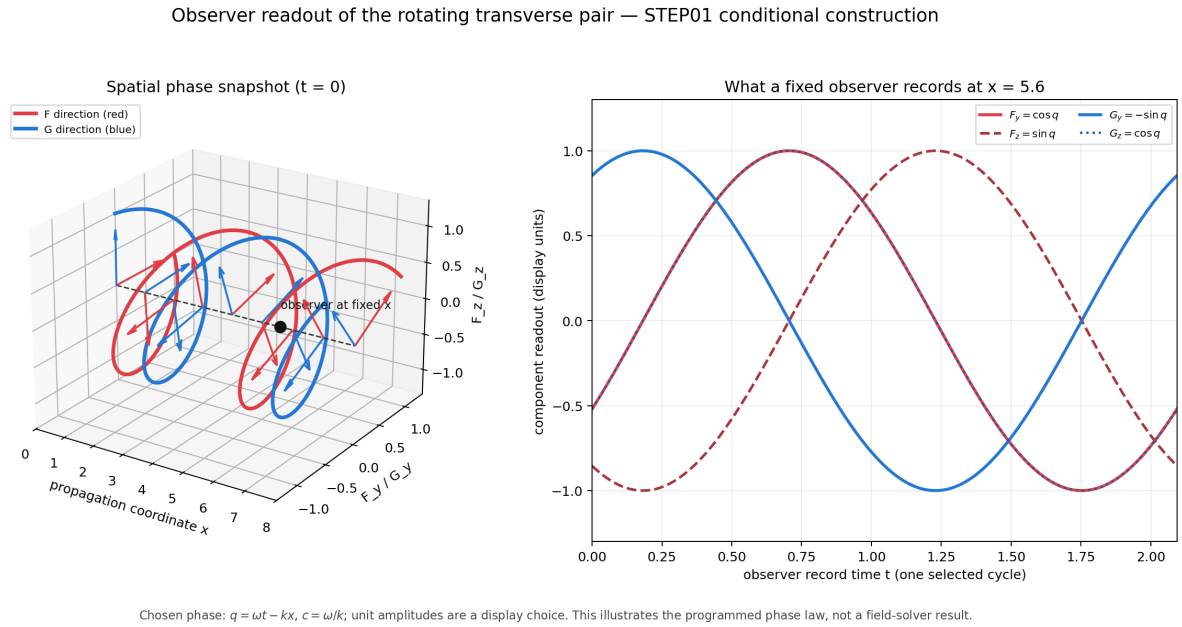

Figure 4: STEP01 spatial profile (left) and time-ordered field-component record at a fixed observation point (right), calculated from the specified traveling-phase law. Source: `STEP01_Two_Observer_Simulations_v1.zip`.

demonstration, $\theta = \omega t - kx$, with $\omega = 3$, $c = 2$, $k = 1.5$, $x_{\text{obs}} = 5.6$, and unit plotting amplitudes, all in normalized units.

A recurrence can function as a local tick when successive states are distinguishable and the observer has an ordering and memory rule. The STEP01 phase-unwrapping check recovers four cycles with suitable sampling, whereas one sample per revolution aliases them into identical records. This illustrates the operational role of sampling in internal cycle counting and connects the proposal to broader relational-clock questions [5, 6].

8 Arc-phase geometry and spatial counting

Consider the author's mathematical example of 100 concentric rings, each assigned $N = 360$ equal angular recurrence intervals. One interval has

$$\Delta\phi = \frac{2\pi}{N}, \qquad \ell_{\text{arc},i} = r_i \Delta\phi, \qquad \ell_{\text{chord},i} = 2r_i \sin\left(\frac{\pi}{N}\right). \tag{17}$$

At common angular rate Ω, each ring has tangential speed $r_i\Omega$ and interval duration $\Delta\phi/\Omega$. This radius dependence motivates the proposal to use arc phase intervals as an intrinsic local measure of length.

Place two vertical parallel lines at $x = 0$ and $x = d$, with $r_i \geq d$, and select the upper-right arc of each circle. The angular interval subtended between the lines, its arc length, and the spatial phase-interval count are

$$\Delta\phi_i = \arcsin(d/r_i), \qquad S_i = r_i \arcsin(d/r_i), \qquad \mathcal{N}_i = \frac{N}{2\pi} \arcsin(d/r_i). \tag{18}$$

For $r_i/d = 1, 2, 4$, respectively, $\mathcal{N}_i = 90, 30, 14.4775$ intervals. The same straight gap therefore subtends different *ring-owned arc phase counts*.

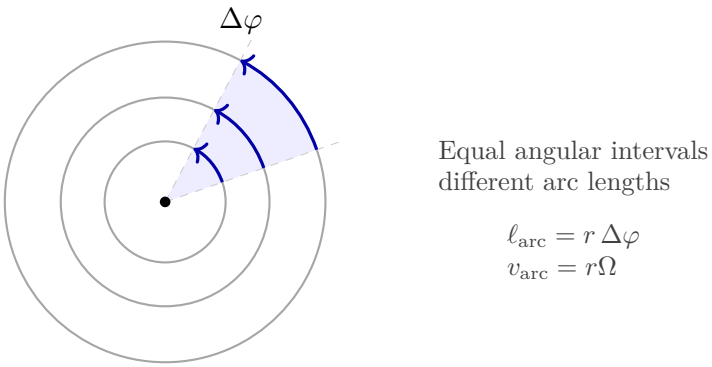

Figure 5: Equal angular progression across rings of different radii. The wedge is enlarged for visibility; arc lengths scale with radius at fixed angular increment.

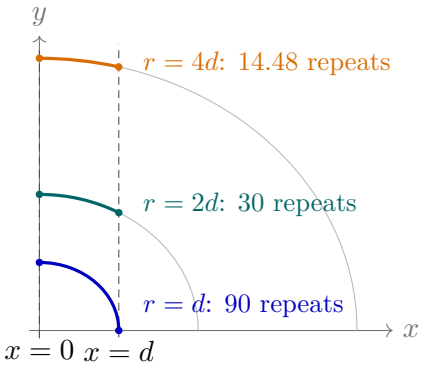

Figure 6: Arc portions between fixed parallel lines for three concentric rings, with 360 assigned angular intervals per revolution. The indicated values count spatial phase intervals along the selected arcs.

Noninteger values denote fractional phase intervals. At common N and Ω, the fixed-mark passage rate is $N\Omega/(2\pi)$ on every ring; spatial arc counts therefore vary with radius even as the temporal recurrence rate remains uniform.

Arc length, transverse radius, axial wavelength and observer-reported straight distance are distinct quantities. Connecting Eq. (17) to the reference Gam_L would require an angular-to-axial mapping and a suitable measurement model. The native-unit convention in Eq. (15) remains well defined in the meantime.

9 Transverse profiles and helical relations

A smooth illustrative transverse envelope may be chosen as

$$A(\rho) = A_0 e^{-\kappa\rho^2/2}, \qquad B(\rho) = B_0 e^{-\kappa\rho^2/2}, \qquad \rho = \sqrt{y^2 + z^2}, \quad \kappa > 0. \tag{19}$$

Because this profile is independent of ξ, τ, it satisfies the axial equations (13); its logarithmic radial gradient is $-\partial_\rho \ln A = \kappa\rho$. The Gaussian serves as one admissible profile within a family of transverse envelopes, with κ specified as a profile parameter.

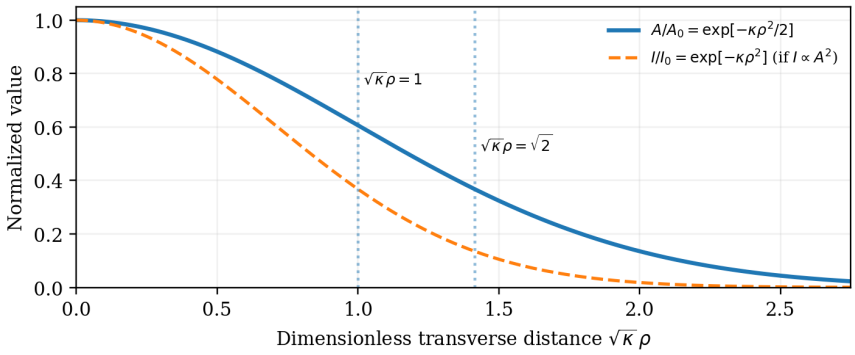

Figure 7: Illustrative Gaussian transverse amplitude and its squared-amplitude profile, using $I \propto A^2$ as a plotting relation.

A separately proposed helical comparison with radius r, pitch p and constant pitch angle α gives

$$\tan\alpha = \frac{2\pi r}{p}, \qquad p = \frac{2\pi r}{\tan\alpha}, \qquad \frac{p_2}{p_1} = \frac{r_2}{r_1} \quad (\alpha \text{ fixed}). \tag{20}$$

The constant-angle relation gives $p \propto r$. Identifying the geometric pitch p with a local wavelength would then yield a wavelength–radius scaling. Such an identification, and any dependence on source-to-observer distance, require separate physical relations; ρ in Eq. (19) remains a transverse coordinate.

10 CMB temperature–redshift prediction and observational comparison

The helical wave construction permits a definite temperature–redshift calculation under an explicit geometric-to-spectral correspondence. We evaluate its resulting curve against published reconstructed CMB temperatures across $0.037 \le z \le 6.34$. The calculation and its independent observational inputs are shown separately for reproducibility.

10.1 From local wave geometry to a temperature relation

For the constant-angle helical construction of the preceding helical calculation, the geometric pitch is $p_{\mathrm{helix}} = 2\pi r/\tan\alpha$ and hence $p_{\mathrm{helix}} \propto r$ at fixed α. We explore the correspondence in which the axial pitch tracks the wavelength of the relevant propagating wave. With emitted and observed wavelength measurements made in their respective frames,

$$1 + z \equiv \frac{\lambda_{\mathrm{obs}}}{\lambda_{\mathrm{em}}} \quad \longleftrightarrow \quad \frac{r_{\mathrm{obs}}}{r_{\mathrm{em}}} \quad \text{(under the stated wave–pitch identification).} \tag{21}$$

Equivalently $r_{\mathrm{em}}/r_{\mathrm{obs}} = 1/(1+z)$. Equation (21) specifies the bridge from the radius ratio in the local helical geometry to the redshift readout. The redshifts used below are independently reported observational inputs; the comparison therefore tests the temperature relation at these input values, rather than a model-generated catalogue of source redshifts.

For a blackbody population with occupation number $n(\nu, T) = [\exp(h\nu/(k_{\mathrm{B}}T)) - 1]^{-1}$, suppose the transported occupation number is preserved under a common frequency shift $\nu_{\mathrm{em}} = (1+z)\nu_{\mathrm{obs}}$. The same distribution then obeys

$$n_{\mathrm{obs}}(\nu_{\mathrm{obs}}) = n_{\mathrm{em}}((1+z)\nu_{\mathrm{obs}}, T_{\mathrm{em}}) = n_{\mathrm{P}}\left(\nu_{\mathrm{obs}}, \frac{T_{\mathrm{em}}}{1+z}\right). \tag{22}$$

Identifying the locally measured present epoch with $z = 0$ yields the conditional temperature relation

$$\boxed{T_{\mathrm{model}}(z) = T_0(1+z), \qquad T_0 = 2.725\ \mathrm{K}.} \tag{23}$$

The normalization T_0 is a present-day measured reference fixed before evaluation of the distant-temperature data. The wave–pitch correspondence and preservation of blackbody occupation numbers are the physical inputs for this application. The same temperature scaling is obtained in adiabatic standard cosmology [9, 10]; comparing both descriptions requires observables beyond their common temperature law.

10.2 Empirical-input parity for the CMB calculation

Here the observational target is the reconstructed CMB temperature as a function of a *reported* source redshift. Two calculations can be put on the same footing: the local-wave correspondence of Eq. (21) with occupation-number transport, and the conventional adiabatic blackbody temperature law in standard cosmology [9, 10]. Both yield the expression in Eq. (23), while their physical descriptions of wavelength evolution differ. We inventory which inputs are measurements and which are theoretical premises before comparing the residuals.

Thus the *empirical input budget for the plotted temperature curve* is matched: one locally measured temperature normalization and the same reported redshifts, with the same 45 remote temperature estimates reserved as the evaluation set. This is a statement about this particular observable, not a comparison of the total premises of the underlying cosmological theories. The 45 rows represent 45 published estimates, including binned cluster measurements; the displayed diagonal score uses symmetrized uncertainties and does not establish 45 statistically independent experiments. The observational reduction pipelines have their own calibrations and modeling assumptions; these are properties of the shared published data and are not silently counted as independent inputs to one model alone.

The common $p = 1$ temperature relation makes this an informative *compatibility* result for the local-wave application but not a discriminating likelihood ratio between the two mechanisms. The post-hoc exponent scan is a separate diagnostic and is not added to the set of independently fixed predictions. Conversely, neither the external redshift values nor the measured present-day T_0 are evidence of numerical fitting to the 45 remote temperature targets.

Table 3: Matched empirical-input ledger for a fixed $T(z)$ calculation. "Target-only" means absent from the formula and parameter selection, although its reported value is subsequently used to compute a residual.

Input or premise (type)	Zero Theory local-wave calculation	Standard adiabatic CMB comparator
Present temperature T_0 (empirical reference)	Measured 2.725 K fixed before the 45 comparisons.	Same measured reference temperature; no extra normalization from remote T_i.
Source redshifts z_i (empirical input)	The 45 published redshifts enter as arguments of $T_0(1+z_i)$.	The same 45 redshifts enter the same temperature law.
Distant reconstructed T_i and errors (target-only)	All 45 used to calculate residuals after the fixed curve is specified.	Same targets and reported uncertainties for a matched score.
Wavelength-evolution premise (theoretical)	Fixed-angle helix pitch $p \propto r$, its specified physical wavelength identification, and the radius/redshift readout.	Cosmological scale-factor redshift, $1+z = a_0/a$, in the expanding-space description.
Spectrum-evolution premise (theoretical)	Preservation of blackbody occupation under the specified common frequency shift.	Initial blackbody and adiabatic photon evolution in the standard setting.
Parameters fitted to these 45 temperatures	None in the principal $p=1$ comparison.	None for the fixed standard $p=1$ curve.
Local Gam_L, local Tick_L or c_{cal}	Not numerical inputs to the 45 temperature predictions.	Not numerical inputs to the fixed $T_0(1+z)$ curve.

10.3 Independent-data comparison protocol

We evaluated Eq. (23) at all 45 redshifts listed in Table 1 of Gelo *et al.* [9]: 18 thermal Sunyaev–Zel'dovich (tSZ) redshift-bin estimates from Planck clusters, 12 tSZ estimates from SPT clusters, and 15 spectroscopic or molecular/atomic estimates at larger redshifts. The compilation reports *reconstructed* radiation temperatures and published one-standard-deviation uncertainties, not 45 separate raw photon-count measurements. Neither the published distant temperatures nor their error bars enter Eq. (23) or its fixed normalization.

For entry i, write $\sigma_{i,+}$ and $\sigma_{i,-}$ for the upper and lower quoted one-standard-deviation errors. The symmetrized standard deviation and descriptive residual are

$$\bar{\sigma}_i = \frac{\sigma_{i,+} + \sigma_{i,-}}{2}, \quad \Delta_i = T_{i,\mathrm{obs}} - T_0(1+z_i), \quad \nu_i = \frac{\Delta_i}{\bar{\sigma}_i}, \quad Q_{\mathrm{diag}} = \sum_{i=1}^{45} \nu_i^2. \tag{24}$$

The full per-row inputs and outputs appear in Appendix A. This deliberately simple diagonal comparison does not use the covariance of cluster stacks, a full spectral inference likelihood or inter-publication systematics; hence Q_{diag} is a descriptive consistency statistic rather than a likelihood-based model-selection measure.

10.4 Results and checks

The fixed curve yields

$$\boxed{45/45 \text{ entries within } 2\bar{\sigma}_i, \qquad 36/45 \text{ within } \bar{\sigma}_i, \qquad Q_{\mathrm{diag}} = 25.403128.} \tag{25}$$

The average contribution is $Q_{\mathrm{diag}}/45 = 0.564514$, and the largest absolute standardized residual is 1.870 at $z = 0.525$. The curve and measurement uncertainties are displayed in Fig. 8. These results constitute a positive numerical compatibility result for the stated conditional relation.

As a supplementary shape-sensitivity analysis, we also evaluated $T_p(z) = T_0(1+z)^p$ with the same fixed T_0, obtaining $Q_{\mathrm{diag}}(p) = 75.945,\ 35.435,\ 25.403,\ 48.622,\ 108.142$ for $p =$

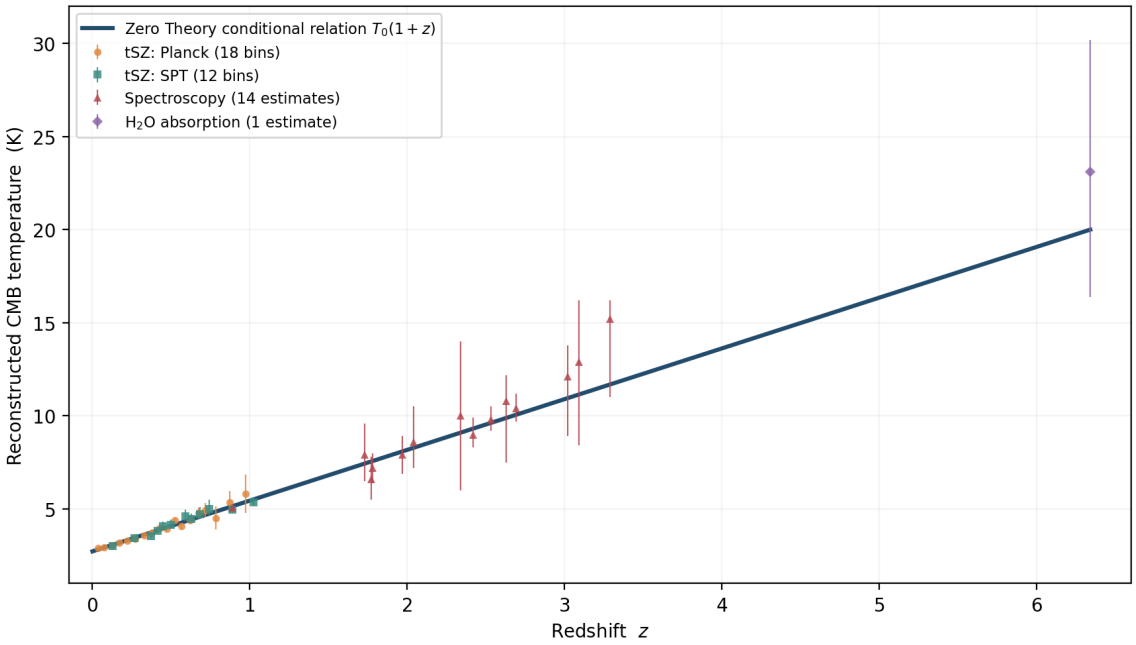

Figure 8: Comparison of Eq. (23) with 45 reconstructed CMB temperature estimates, including their published asymmetric one-standard-deviation uncertainties. Data transcribed from Gelo et al. (2022), Table 1 [9], with attribution under CC BY 4.0. The reference curve uses $T_0 = 2.725$ K fixed in advance. The 18 Planck and 12 SPT entries are binned cluster results, whereas the other 15 entries are spectroscopic estimates.

0.90, 0.95, 1.00, 1.05, 1.10, respectively. The post-hoc diagonal minimum is approximately $p = 0.9907$; this is a sensitivity fit performed *after* access to the measurements, not another independent confirmation. Figure 9 illustrates the sensitivity.

A known source-level redshift discrepancy is explicitly retained: one row appears at $z = 0.332$ in Gelo et al. Table 1, while a related compilation gives $z = 0.322$ for the same quoted temperature. We retain Gelo et al.'s $z = 0.332$ for source fidelity; omission of that entry produces $Q_{\mathrm{diag}} \simeq 23.708$ for 44 rows, with all 44 individually within $2\bar{\sigma}$. This source-note sensitivity does not alter the primary comparison.

11 Integrated results

The study yields distinct mathematical, computational, and observational results. Tables 2 and 3 separately document the general starting structures and the specific measured inputs of the CMB comparison. Table 4 identifies the input for each calculation and the quantity it determines, providing a concise guide to the detailed derivations above.

The delayed-matching and mirror results offer a detailed geometrical specification of the proposed local pair. The CMB comparison provides an observational check of a fixed temperature law, accompanied by a complete 45-row audit trail. The Gaussian Maxwell test supplies an independent consistency constraint on one possible electromagnetic interpretation. Together, the results indicate which relations are established by geometry, which depend on a declared transport rule, and which have been compared with published observations.

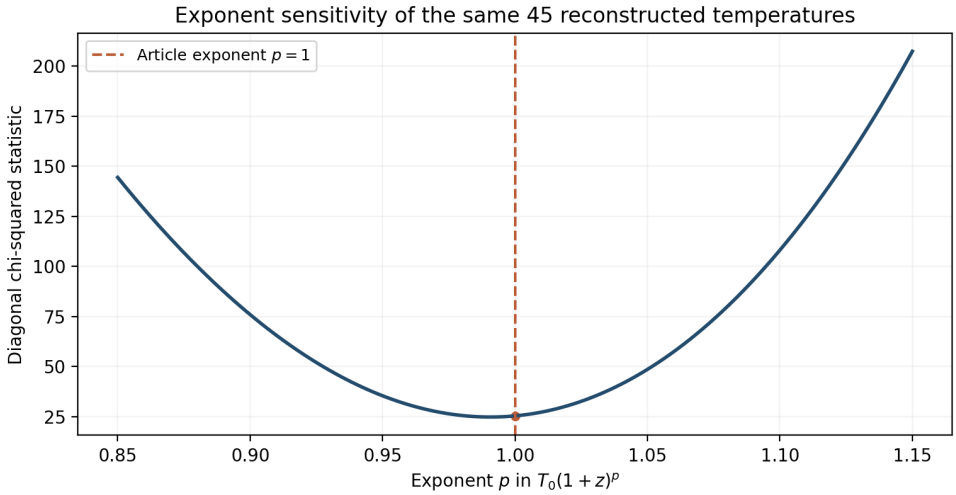

Figure 9: Diagnostic sensitivity of the same 45 entries to an exponent p in $T_0(1+z)^p$, with fixed T_0. This illustrates that the observations constrain the curve's shape. The fitted exponent is a post-hoc comparison and is distinct from the predeclared $p = 1$ curve.

Table 4: Principal findings, listed by model ingredient and calculated result.

Model element	Calculated finding	Basis / interpretation
Rotating transverse pair	Orthogonality and exact differential identities	Orthonormal transverse basis; specified amplitudes and differentiable phase.
Selected traveling phase	First-order axial transport identities	Uniform characteristic in local normalized coordinates.
Reference wavelength and period	Wave-owned local step and tick; unit-speed convention	One spatial cycle and its completion period.
STEP01 observer construction	Distinct spatial and fixed-position temporal records	Prescribed phase and observer sampling sequence.
Concentric-ring geometry	Radius-dependent arc length and strip phase count	Euclidean arc geometry with assigned angular intervals.
Two-pole delayed pursuit	Exact quarter-cycle matching condition	Rigid perpendicular planes and prior-location matching.
Hinge feedback example	86.3% reduction in average positional mismatch	Chosen gradient response; two modeled phase cycles.
Facing-axis mirror pair	Antiparallel axes; exact reflection and delayed position identities	Specified local frames and mirrored phase schedule.
Transverse Gaussian	Compatible profile under axial transport	Axially invariant envelope with free width parameter.
Constant-angle helix	Pitch scales with helix radius	Fixed pitch angle.
CMB temperature relation	$T_{\mathrm{CMB}} = T_0(1+z)$ and 45/45 within $2\bar{\sigma}$; $Q_{\mathrm{diag}} = 25.403$	Wave–pitch correspondence; blackbody transport; published reconstructed temperatures.
Three-dimensional Maxwell check	Nonzero divergences for one transverse-only Gaussian field choice	Source-free field consistency test of a specified ansatz.

12 Electromagnetic consistency checks

Maxwell electrodynamics provides a well-established comparator once the abstract pair is mapped to measurable $\mathbf{E}, \mathbf{B}$. In a homogeneous plane-wave sector, an appropriately chosen mapping and phase relation allow selected rotating transverse configurations to satisfy source-free Maxwell evolution. The mapping is a separate assumption from the geometric identities of Sec. 4.

The earlier v0.5 manuscript also tested a *particular* 3D Gaussian identification,

$$\mathbf{E} = (0, A\cos\theta, A\sin\theta), \qquad \mathbf{B} = (0, -A\sin\theta, A\cos\theta)/c, \qquad A = A_0 e^{-\kappa(y^2+z^2)/2}. \tag{26}$$

With $\theta = \omega(t - x/c)$, its divergences are

$$\nabla\cdot\mathbf{E} = -\kappa A(y\cos\theta + z\sin\theta), \qquad \nabla\cdot\mathbf{B} = \frac{\kappa A}{c}(y\sin\theta - z\cos\theta). \tag{27}$$

The divergences are generally nonzero, so this transverse-only Gaussian ansatz fails the complete three-dimensional, source-free Maxwell constraints. The test identifies a limitation of this specific field construction and motivates consideration of longitudinal components or a different beam solution.

13 Discussion

The present construction links local wave geometry to an operational measurement scheme. Its strongest mathematical result is the exact condition for quarter-cycle-delayed matching in a perpendicular two-pole ring model. The two-structure extension realizes that condition with inward-facing, antiparallel axes and preserves mirror symmetry. The wave-pair transport formulation and observer examples provide complementary descriptions of the same organized recurrence: one as a spatial profile, the other as a recorded cycle sequence. The arc-count calculation additionally shows how radial geometry can change a spatial phase measure without changing a common recurrence rate.

The temperature–redshift application supplies a separate empirical result. The fixed curve $T_0(1+z)$ is compatible at the two-standard-uncertainty level with all 45 reconstructed CMB temperatures in the adopted compilation, with a descriptive diagonal residual sum of 25.403. Because the distant temperatures were not used to normalize or fit the principal curve, this is a direct comparison of a specified relation against reported measurements. The same scaling is also predicted by standard adiabatic cosmology, so the comparison supports the common functional law; it does not by itself select between the proposed geometric interpretation and the established cosmological mechanism. Correlations and astrophysical inference systematics should be included in any subsequent joint likelihood analysis.

The framework uses several clearly identified inputs: a computational phase order, a selected traveling characteristic, a wave–pitch correspondence, blackbody occupation transport, and a particular feedback controller for the ring example. A physical field map connecting ring trajectories to $\mathbf{F}, \mathbf{G}$ and measured $\mathbf{E}, \mathbf{B}$, together with a dynamical source law, would permit a more stringent mechanistic test. These are focused extensions of the present results rather than conditions on reporting the established geometrical and observational checks.

14 Conclusion

We have formulated and tested a local-wave construction with explicit geometry, operational units, and an observational application. Exact transverse-pair relations, a closed-form delayed-orientation condition, an 86.3% numerical pursuit-error reduction under a specified controller,

and a reproducible antiparallel mirror-pair realization are obtained within the stated geometry. Wave-based ruler and clock definitions, observer cycle readouts, and arc-phase calculations supply the associated measurement structure.

With a specified helical pitch–wavelength correspondence and blackbody transport, the framework produces $T_{\mathrm{CMB}}(z) = T_0(1+z)$. Using a pre-fixed $T_0 = 2.725$ K, all 45 reconstructed temperatures in the Gelo et al. compilation fall within two quoted standard uncertainties of this curve; the diagonal residual sum is 25.403. Source-attributed observations, numerical errors, model values and code are included for independent reproduction. The combination of exact geometric results and a documented observational compatibility test establishes a concrete basis for further work on physical source dynamics and measurable field mappings.

A Complete 45-entry CMB temperature comparison and provenance

Table 5 reproduces the numerical entries needed to check the observational result. The redshifts, reconstructed temperatures and errors are adapted from Gelo et al. (2022), Table 1, originally published under Creative Commons Attribution 4.0 (https://creativecommons.org/licenses/by/4.0/). Attribution: L. Gelo, C.J.A.P. Martins, N. Quevedo and A.M.M. Vieira, *Physics Letters B* **835** (2022) 137570, https://doi.org/10.1016/j.physletb.2022.137570. The 2022 paper's reference numbers for each source are included in the "Gelo ID" column; [10] denotes the Planck SZ stacks, [11] SPT SZ stacks, and other numbers refer to spectroscopic studies as enumerated in that publication. "Gelo ID" is a bibliographic index in the original compilation, independent of this manuscript's reference numbering. All observed values are quoted in kelvin. For compactness, T_{mod} and ν_i are rounded in this printed table; the reproducibility CSV and Python retain full calculation precision.

Table 5: All 45 published temperature entries and model comparisons. Uncertainty columns are the original upper/lower one-sigma values; ν_i uses their arithmetic mean. CC BY 4.0 source attribution above.

No.	z	T_{obs}	σ_+	σ_-	T_{mod}	ν_i	Gelo ID
1	0.037	2.888	0.041	0.041	2.826	+1.516	10
2	0.072	2.931	0.020	0.020	2.921	+0.490	10
3	0.125	3.059	0.034	0.034	3.066	-0.195	10
4	0.129	3.010	0.140	0.110	3.077	-0.532	11
5	0.171	3.197	0.032	0.032	3.191	+0.188	10
6	0.220	3.288	0.035	0.035	3.325	-1.043	10
7	0.265	3.440	0.160	0.130	3.447	-0.049	11
8	0.273	3.416	0.040	0.040	3.469	-1.323	10
9	0.332	3.562	0.052	0.052	3.630	-1.302	10
10	0.371	3.530	0.180	0.140	3.736	-1.287	11
11	0.377	3.717	0.065	0.065	3.752	-0.543	10
12	0.416	3.820	0.190	0.150	3.859	-0.227	11
13	0.428	3.971	0.073	0.073	3.891	+1.092	10
14	0.447	4.090	0.250	0.190	3.943	+0.668	11
15	0.471	3.943	0.113	0.113	4.008	-0.579	10
16	0.499	4.160	0.270	0.200	4.085	+0.320	11
17	0.525	4.380	0.120	0.120	4.156	+1.870	10
18	0.565	4.075	0.157	0.157	4.265	-1.208	10
19	0.590	4.620	0.360	0.260	4.333	+0.927	11
20	0.619	4.404	0.195	0.195	4.412	-0.040	10
21	0.628	4.450	0.310	0.230	4.436	+0.051	11
22	0.676	4.779	0.279	0.279	4.567	+0.759	10
23	0.681	4.720	0.390	0.270	4.581	+0.422	11
24	0.718	4.933	0.371	0.371	4.682	+0.678	10
25	0.742	5.010	0.490	0.330	4.747	+0.642	11
26	0.783	4.515	0.621	0.621	4.859	-0.553	10

Table 5 continued

No.	z	$T_{\rm obs}$	σ_+	σ_-	$T_{\rm mod}$	ν_i	Gelo ID
27	0.870	5.356	0.617	0.617	5.096	+0.422	10
28	0.887	4.970	0.240	0.190	5.142	-0.800	11
29	0.890	5.080	0.100	0.100	5.150	-0.703	17
30	0.972	5.813	1.025	1.025	5.374	+0.429	10
31	1.022	5.370	0.220	0.180	5.510	-0.700	11
32	1.730	7.900	1.700	1.400	7.439	+0.297	12
33	1.770	6.600	1.200	1.100	7.548	-0.825	12
34	1.780	7.200	0.800	0.800	7.576	-0.469	18
35	1.970	7.900	1.000	1.000	8.093	-0.193	19
36	2.040	8.600	1.900	1.400	8.284	+0.192	12
37	2.340	10.000	4.000	4.000	9.101	+0.225	4
38	2.420	9.000	0.900	0.700	9.319	-0.399	12
39	2.530	9.800	0.700	0.600	9.619	+0.278	12
40	2.630	10.800	1.400	3.300	9.892	+0.386	12
41	2.690	10.400	0.800	0.700	10.055	+0.460	12
42	3.020	12.100	1.700	3.200	10.954	+0.468	20
43	3.090	12.900	3.300	4.500	11.145	+0.450	12
44	3.290	15.200	1.000	4.200	11.690	+1.350	12
45	6.340	23.100	7.100	6.700	20.002	+0.449	5

The original source transcribes 30 tSZ bin averages and 15 spectroscopy-based estimates. Asymmetric errors are retained as printed and are symmetrized only in the computation of $Q_{\rm diag}$; the plotting script draws the unequal upper and lower bars. The data include an intentional original-source choice at row 9: $z = 0.332$ from Gelo et al. Table 1. Remote temperature inference also depends on astrophysical models and possible shared measurement information. The original five-point CO comparison is preserved separately in Appendix C; it is historical and is not added to the 45-point total as independent data.

B CMB numerical reproducibility and evidence map

The supplemental release supplies the complete script `reproduce_cmb_45.py`, the exact input table `45_observations_Gelo2022_comparison.csv`, and `statistics_reproduced.json` with unrounded results and tests. Running `python code/reproduce_cmb_45.py` from any directory with Python, NumPy and Matplotlib installed recreates the plotted diagnostics and summary scores. Values $z_i, T_{{\rm obs},i}, \sigma_{i,\pm}$ originate in Gelo et al.'s Table 1; the remaining columns are generated by Eq. (23) and Eq. (24). No remote temperatures are fitted in the principal $p = 1$ calculation. We also include the previously reported 100 sampled model evaluations; these are curve samples, not 100 independent observations.

For long-term traceability, the supplement includes a research evidence ledger mapping the result `ZT-CMB-45-COMPAT-20261116` to the model-version source, DOI and Table 1, copied source values, checksum manifest, calculation code, and derived graphics. For primary-source verification, the publisher DOI, the accessible arXiv:2211.05377 record, the author-attributed transcription and the local row-wise audit ledger are provided in the supplement.

C Earlier five-point CO demonstration

The earlier five-point score is $Q = \sum_i [(T_{{\rm CO},i} - T_0(1 + z_i))/\sigma_i]^2$. It uses a diagonal approximation and does not reconstruct original spectral likelihoods or full systematic covariance. Published FIRAS products contain calibration/processing assumptions; a model reconstructed from their inserted blackbody baseline is not independent confirmation [12].

Table 6: Earlier published reconstructed CO-excitation temperatures and the assumed $T_0(1+z)$ comparison curve.

z	T_{CO} (K)	adopted σ (K)	T_{model} (K)	residual (%)
1.7293	7.50	1.60	7.4373	+0.84
1.7738	7.80	0.70	7.5586	+3.19
2.6896	10.50	0.80	10.0542	+4.43
2.4184	9.15	0.70	9.3151	-1.77
2.0377	8.60	1.10	8.2777	+3.89

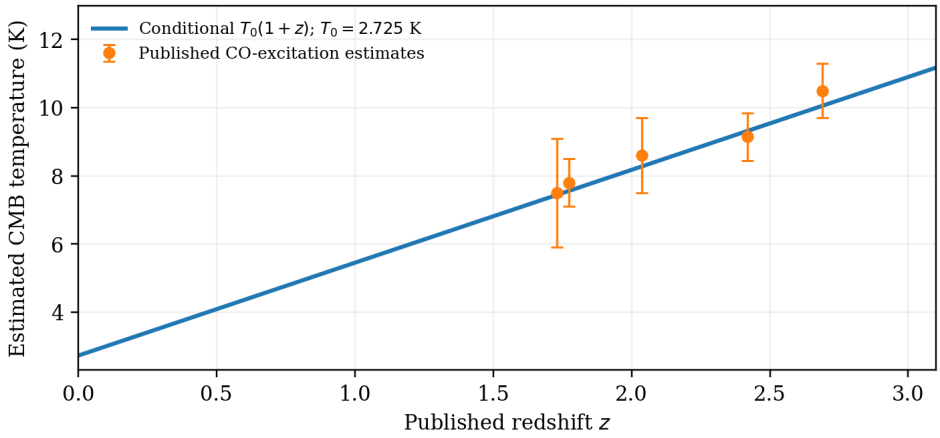

Figure 10: Five published CO-excitation temperature estimates and the entered $T_0(1+z)$ curve. The same redshift variable enters the comparison assumption.

D Ring-geometry reproducibility

Independent symbolic manipulation verifies Eq. (4) and the matching condition. A grid of 2001 phases over two cycles gives locked-track mean mismatch $0.90057R$, consistent with the archived value $0.90055R$ at its native discretization. The exact $\alpha = -s$ solution yields floating-point-level coincidence; a periodic modulation and alternative winding branch also give mismatches below $10^{-14}R$, confirming nonuniqueness. The 86.3% feedback improvement comes from the earlier controller run, which assumes its response law. Source code, JSON outputs and numerical settings are included in the reproducibility package.

E Facing-axis numerical verification

The supplied `build_facing_axes.py` declares $d = 1.65$, $R = 1$, $\delta = \pi/2$ and samples 1601 dimensionless phase labels for its coordinate checks. Those values do not determine an SI wavelength, frequency or field strength. Its recorded JSON checks give $\|\mathbf{n}_+ + \mathbf{n}_-\| = 0$, direction-to-opposite-center products 3.3 on each side, mirror errors 0, delayed-site mismatch 0, pole drift $\simeq 1.22 \times 10^{-16}$ and plane nonorthogonality $\lesssim 5.0 \times 10^{-16}$. The animation frames and HTML permit inspection of the *declared* kinematics but are not new independent dynamical tests. A small independent checkpoint in this package verifies the reflection, lag and perpendicularity identities without requiring the animation writer.

The original single-hinge test and the later two-structure facing-axis display use separate parameterizations. Their sources are retained independently for versioned reproduction. A particle-formation

application would require a further map to physical, frame-defined degrees of freedom and measurable charge, mass and conservation quantities.

F Computational sources and provenance

The calculations draw on the TFPT manuscript v0.5, the Zero Theory cumulative electromagnetic study, the STEP01 observer simulation, the v0.7 reactive-ring model and the author-corrected facing-axis v3 construction. The editable source package preserves Python implementations, figures, input parameters, archived outputs and numerical checkpoints. The independent geometry checks reproduce algebraic relations under the specified inputs; they are distinct from experimental measurements.

Two negative controls remain part of the record: the source-free Maxwell test fails for the specified transverse-only Gaussian field ansatz, and a codirected-axis version fails the intended face-to-face orientation criterion. The two-dimensional fountain/vortex advection study is a separate analogy with imposed sink circulation; it is not included as evidence of black-hole dynamics or TFPT source law. The present editorial revision preserves the stated numerical inputs, geometric results, observational table and source-to-result audit records.

References

[1] S. M. H. Emamifar, *Zero Theory: Chapter One—The Opening Question*, Zero Theory Research Program / IRCBHC, author-provided unpublished manuscript (2026).

[2] S. Surya, "The causal set approach to quantum gravity," *Living Rev. Relativ.* **22**, 5 (2019). doi:10.1007/s41114-019-0023-1.

[3] S. Gielen and L. Sindoni, "Quantum Cosmology from Group Field Theory Condensates: a Review," *SIGMA* **12**, 082 (2016). doi:10.3842/SIGMA.2016.082.

[4] M. Van Raamsdonk, "Building up spacetime with quantum entanglement," *Gen. Relativ. Gravit.* **42**, 2323–2329 (2010), preprint arXiv:1005.3035.

[5] D. N. Page and W. K. Wootters, "Evolution without evolution: Dynamics described by stationary observables," *Phys. Rev. D* **27**, 2885–2892 (1983). doi:10.1103/PhysRevD.27.2885.

[6] C. Rovelli, "Partial observables," *Phys. Rev. D* **65**, 124013 (2002). doi:10.1103/PhysRevD.65.124013.

[7] M. Levin and X.-G. Wen, "Colloquium: Photons and electrons as emergent phenomena," *Rev. Mod. Phys.* **77**, 871–879 (2005). doi:10.1103/RevModPhys.77.871.

[8] P. Noterdaeme et al., "The evolution of the cosmic microwave background temperature: measurements of T_{CMB} at high redshift from carbon monoxide excitation," *Astron. Astrophys.* **526**, L7 (2011). doi:10.1051/0004-6361/201016140.

[9] L. Gelo, C.J.A.P. Martins, N. Quevedo, and A.M.M. Vieira, "Cosmological impact of microwave background temperature measurements," *Physics Letters B* **835**, 137570 (2022), Table 1. doi:10.1016/j.physletb.2022.137570. Open access CC BY 4.0; arXiv:2211.05377.

[10] C.J.A.P. Martins and A.M.M. Vieira, "Current and future cosmological impact of microwave background temperature measurements," *Physics of the Dark Universe* **44**, 101494 (2024). doi:10.1016/j.dark.2024.101494.

[11] D.A. Riechers et al., "Microwave background temperature at a redshift of 6.34 from H_2O absorption," *Nature* **602** (2022). doi:10.1038/s41586-021-04294-5.

[12] NASA/GSFC LAMBDA, "FIRAS monopole spectrum: description and calibrated data," `https://lambda.gsfc.nasa.gov/product/cobe/firas_monopole_spect.html`.

[13] A. Einstein, "Zur Elektrodynamik bewegter Körper," *Annalen der Physik* **17**, 891–921 (1905). doi:10.1002/andp.19053221004.

[14] J. C. Maxwell, "A Dynamical Theory of the Electromagnetic Field," *Philos. Trans. R. Soc. Lond.* **155**, 459–512 (1865). doi:10.1098/rstl.1865.0008.